

**Structure and magnetism in synthetic pyrrhotite  $\text{Fe}_7\text{S}_8$ : A powder neutron-diffraction study**Anthony V. Powell,<sup>1,\*</sup> Paz Vaquero,<sup>1</sup> Kevin S. Knight,<sup>2</sup> Laurent C. Chapon,<sup>2</sup> and Rodolfo D. Sánchez<sup>3</sup><sup>1</sup>*Department of Chemistry, Heriot-Watt University, Edinburgh EH14 4AS, United Kingdom*<sup>2</sup>*ISIS Facility, Rutherford Appleton Laboratory, Didcot, Oxfordshire OX11 0QX, United Kingdom*<sup>3</sup>*Centro Atómico Bariloche, 8400 Bariloche (RN), Argentina*

(Received 20 October 2003; revised manuscript received 29 March 2004; published 15 July 2004)

The relationship between structural and magnetic properties in stoichiometric pyrrhotite  $\text{Fe}_7\text{S}_8$  has been investigated using variable-temperature neutron-diffraction data. Below its magnetic ordering temperature,  $T_N = 598(5)$  K,  $\text{Fe}_7\text{S}_8$  exhibits a monoclinic 4C structure, related to that of NiAs, in which fully occupied cation layers alternate with cation-deficient layers. The magnetic structure consists of ferromagnetically aligned layers, with antiferromagnetic coupling of adjacent layers. The ordered moment of  $3.16(1)\mu_B$  at 11 K is directed at an angle of  $29^\circ$  to the layers. The magnetic transition is accompanied by a structural transformation from the monoclinic 4C structure to a hexagonal cation-deficient NiAs structure, in which the vacancies are statistically distributed between all layers. Although the 4C structure is recovered on cooling through the magnetic transition, the resultant phase exhibits a significant degree of intralayer cation disorder.

DOI: 10.1103/PhysRevB.70.014415

PACS number(s): 75.25.+z, 64.70.Kb, 61.66.Fn, 75.30.Kz

**I. INTRODUCTION**

The structures of many binary and ternary transition-metal sulphides are derived from the metal dichalcogenide unit of edge-sharing octahedra. Occupation by cations of a fraction of the octahedral sites between successive pairs of dichalcogenide units generates phases of general formula  $A_xMS_2$ , in which defective and fully occupied layers of cations alternate with anion layers,  $SMSA_xSMS$ . Ordering of vacancies within the defective layer produces a two-dimensional superstructure, the nature of which depends on the vacancy concentration. For example, in the series  $V_x\text{CrS}_2$  ( $0.30 \leq x \leq 0.93$ ) five structurally distinct ternary phases have been identified,<sup>1</sup> some of which exist over extended ranges of composition. Moreover, the extent of vacancy ordering is dependent on preparative conditions, as the high temperatures used in synthesis may lead to order-disorder transitions, involving either or both intralayer or interlayer disordering of vacancies.<sup>2-6</sup>

Chalcogenides of the later transition series elements generally show a more limited range of ordered-defect phases than their counterparts from the beginning of the series. However, in the Fe-S system there is considerable structural complexity for compositions around  $x=3/4$ , much of which is poorly understood.<sup>7</sup> The stoichiometric phase  $\text{Fe}_7\text{S}_8$  (pyrrhotite) adopts a monoclinic structure in which vacancies are confined to every other site in alternate rows of sites within the vacancy layer. The vacancy layers are stacked in an ABCD sequence, quadrupling the unit cell along the stacking direction and leading to its designation as a 4C structure. The phase range of pyrrhotite extends to materials  $\text{Fe}_x\text{S}$ , in the range  $0.875 \leq x \leq 0.95$ . Although the two-dimensional superstructure and ABCD stacking of defect layers persists for iron contents greater than  $x=0.875$ , the strict alternation of full and defective layers is removed and a variety of higher-order  $c$ -axis repeat distances have been identified for iron rich phases.<sup>8</sup>

The magnetic behavior of monoclinic pyrrhotite has been attributed<sup>9</sup> to ferromagnetic alignment of cations within lay-

ers and antiferromagnetic coupling between adjacent layers. The presence of vacancies in alternate layers results in an uncompensated moment, leading to ferrimagnetism. For  $\text{Fe}_x\text{S}$  compositions in the range  $0.87 \leq x \leq 0.88$ , the temperature dependence of the magnetization exhibits typical Weiss-type behavior.<sup>10,11</sup> Pyrrhotites with higher iron contents are characterized by more complex magnetic behavior that depends markedly on composition. Phases with  $x \geq 0.92$  exhibit antiferromagnetism with further phase transitions occurring at lower temperatures, while in the range  $0.89 \leq x \leq 0.92$ , a  $\lambda$  transition is observed<sup>10</sup> in which the magnetization undergoes a sharp rise and subsequent decay on cooling through the relatively narrow temperature range 523–473 K.

Li *et al.* have investigated a series of natural and synthetic pyrrhotites using a combination of transmission electron microscopy<sup>12</sup> high-temperature x-ray diffraction, thermomagnetic measurements, and differential thermal analysis (DTA).<sup>10</sup> For the stoichiometric phase, DTA reveals an unusually large enthalpy change at 583 K and a second weaker feature at ca. 493 K. On the basis of electron diffraction, it was suggested that the feature at 583 K arises from a structural change at the magnetic transition, involving disordering of vacancies in the defect layer only, to yield a  $\text{CdI}_2$ -type structure, while the lower-temperature feature results from a change in stacking sequence from a disordered 4C-type to a disordered 3C-type. However, the monoclinic distortion characteristic of the 4C structure was not discernible in powder x-ray diffraction data for the bulk synthetic sample used in these studies, owing to the presence of stacking faults.<sup>11</sup>

These conclusions concerning the sequence of phase transitions in stoichiometric pyrrhotite were arrived at on the basis of structural and magnetic properties that were investigated independently. In the present work we have exploited the ability of neutron diffraction to probe both structure and magnetism simultaneously. Powder neutron-diffraction data, collected over a wide range of temperatures, provide convincing evidence that in contrast to earlier reports, the 4C structure persists to the magnetic ordering transition and that loss of long-range magnetic order is accompanied by a major structural reorganization, involving vacancy disordering.

## II. EXPERIMENTAL

A mixture of iron and sulphur (both Aldrich 99.9%) powders corresponding to the stoichiometry  $\text{Fe}_7\text{S}_8$  was ground in an agate mortar prior to sealing into an evacuated ( $<10^{-4}$  Torr) silica tube. The mixture was heated at  $500^\circ\text{C}$  for 24 h,  $800^\circ\text{C}$  for 48 h, cooled to  $250^\circ\text{C}$  at  $0.5^\circ\text{C min}^{-1}$ , and held at this temperature for 24 h prior to removal from the furnace. Following regrinding, the material was sealed into a second silica tube and refired at  $800^\circ\text{C}$  for 72 h, cooled to  $250^\circ\text{C}$  at  $0.1^\circ\text{C min}^{-1}$ , held at this temperature for 24 h before cooling at  $0.1^\circ\text{C min}^{-1}$  to  $125^\circ\text{C}$ , at which temperature the sample was removed from the furnace. The nature of the product is critically dependent on the synthesis conditions: both intermediate regrinding and long cooling times were found to be essential for the production of well-ordered phases. Powder x-ray diffraction data for the product were collected with a Philips PA2000 diffractometer using nickel-filtered  $\text{Cu-K}_\alpha$  radiation ( $\lambda=1.5418 \text{ \AA}$ ). Data were collected in step-scan mode using a step size of  $0.02^\circ(2\theta)$  and a counting time of  $10 \text{ s step}^{-1}$ . Magnetization data were collected with a Faraday balance over the temperature range  $275 \leq T(\text{K}) \leq 650$ , using ca. 40 mg of sample sealed into a silica capsule under a pressure of 500 mTorr of dry  $\text{N}_2$ . Data were collected in a measuring field of 100 G both on heating and on cooling at  $2 \text{ K min}^{-1}$ .

Time-of-flight powder neutron-diffraction data were collected at ISIS, Rutherford Appleton Laboratory. The  $\text{Fe}_7\text{S}_8$  product was divided into two portions of ca. 1.5 g, each contained in an evacuated and sealed high-purity boron-free silica ampoule. The ampoule was contained in a thin-walled vanadium can held in a furnace evacuated to a pressure  $<10^{-4}$  Torr for the collection, using the GEM diffractometer,<sup>13</sup> of neutron-diffraction data both on heating and cooling over the temperature range  $298 \leq T(\text{K}) \leq 773$ . The second sample was used for the collection of additional long wavelength data at higher resolution on the Osiris spectrometer<sup>14</sup> operating in its powder-diffraction mode. Using a closed-cycle refrigerator (CCR), data were collected on heating, over the temperature range  $11 \leq T(\text{K}) \leq 413$ . Data collected for an empty silica tube contained in a vanadium can mounted in either the furnace or CCR were used to provide a background, which was subtracted from the experimental data prior to structural refinement. Initial data manipulation and reduction was carried out using Genie<sup>15</sup> spectrum manipulation software. Neutron-diffraction data from four of the GEM detector banks were summed, normalized, and used simultaneously in Rietveld refinement. Data obtained at 11 K and 298 K using Osiris were collected in five time windows, which were then combined to produce diffraction patterns spanning the range  $0.5 \leq d(\text{Å}) \leq 7.0$ , suitable for input into Rietveld refinement. Data at all other temperatures were collected over the more restricted range  $2.7 \leq d(\text{Å}) \leq 6.0$  in order to follow unit-cell parameters and magnetic scattering. All Rietveld refinements were performed using the GSAS package<sup>16</sup> and representational analysis<sup>17</sup> to determine symmetry allowed magnetic structures was carried out using the program SARAH.<sup>18</sup>

## III. RESULTS

Powder x-ray diffraction data could be indexed on the basis of a monoclinic unit cell with unit cell parameters re-

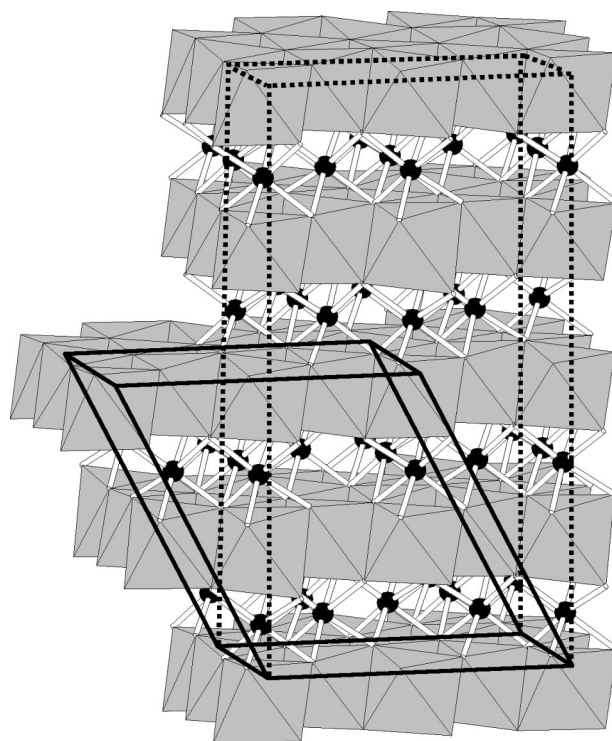


FIG. 1. The ordered-defect structure of 4C pyrrhotite. Cations in the ordered-defect layer are shown as solid circles and cations in the fully occupied layer lie at the center of shaded  $MS_6$  octahedra, which share edges to form a layer of stoichiometry  $MS_2$ . The dashed lines indicate the unit cell described in the space group  $F2/d$  illustrating the four-layer repeat along the  $c$  direction. The solid lines outline the  $C2/c$  unit cell used in the present work.

lated to those of the primitive NiAs unit cell by  $a=2\sqrt{3}a_p$ ;  $b=2a_p$ ;  $c=4c_p$ . This unit cell appears to be consistent with the 4C structure originally proposed by Bertaut<sup>19</sup> and subsequently confirmed by the crystal structure determination of Tokonami *et al.*<sup>20</sup> Both of these earlier reports describe the structure in the unconventional space group  $F2/d$ . This is related to the more conventional  $C2/c$  unit cell which has been used in the present work, through the matrix

$$\begin{pmatrix} 1 & 0 & 0 \\ 0 & 1 & 0 \\ 1 & 0 & 2 \end{pmatrix}.$$

The atomic coordinates in  $C2/c$  are displaced by  $(-0.25, 0.75, 0)$  relative to those of  $F2/d$ . The relationship between the two unit cells is illustrated in Fig. 1. The structure of Tokonami *et al.*<sup>20</sup> described in  $C2/c$  was refined against room-temperature powder x-ray diffraction data, yielding refined lattice parameters of  $a=11.897(2)$ ,  $b=6.8586(9)$ ,  $c=12.891(1)\text{Å}$  and  $\beta=118.036(6)^\circ$ . The refined structure was used as a trial model for analysis of the data collected at 11 K on Osiris. Refinement of the scale factor, background, and lattice parameters, together with an overall thermal parameter, demonstrated that with the exception of a small number of weak features attributable to an  $\text{FeS}_2$  impurity phase (ca. 5 wt %), all reflections may be indexed on a

monoclinic unit cell, with lattice parameters similar to those determined at room temperature. However, several significant discrepancies between observed and calculated intensities are evident at long  $d$  spacings. In particular, the most intense reflection at 5.689 Å, although being crystallographically allowed [indexable as (001) on the basis of the primitive NiAs unit cell] has no significant calculated nuclear contribution. There is a similar mismatch at the multiplet at ca. 2.62 Å. The additional intensity associated with these features is magnetic in origin. Furthermore, the superposition of nuclear and magnetic reflections suggests that the magnetic structure has a propagation vector  $\mathbf{k}=0,0,0$ .

As will be shown below, the magnetic and concomitant structural transitions are first order and hence Landau theory is inapplicable. The removal of the restriction of magnetic ordering to a single symmetry mode that this implies, requires that contributions from secondary modes must be considered. Following the procedure of Bertaut,<sup>21</sup> we have carried out the symmetry analysis within the reference framework of the distorted nuclear structure of the magnetically ordered phase. Having obtained the irreducible representation, the symmetry-allowed single mode representations are screened against the experimental data and then additional contributions from secondary modes are considered. Details of the representational analysis to determine the symmetry-allowed magnetic structures are provided in the Appendix. The magnetic representation associated with an 8( $f$ ) site [Fe(1)–Fe(3)] may be reduced to

$$\Gamma_{\text{mag}}[8(f)] = 3\Gamma_1 + 3\Gamma_2 + 3\Gamma_3 + 3\Gamma_4,$$

while that of a 4( $e$ ) site [Fe(4)] is

$$\Gamma_{\text{mag}}[4(e)] = \Gamma_1 + \Gamma_2 + 2\Gamma_3 + 2\Gamma_4.$$

The one-dimensional irreducible representations  $\Gamma_i$  ( $i=1-4$ ) and the basis vectors spanned by each are defined in the tables in the Appendix. Only  $\Gamma_1$  and  $\Gamma_3$  permit the exclusively ferromagnetic intralayer coupling ( $F_y$  of  $\Gamma_1$  and  $F_x$  and  $F_z$  of  $\Gamma_3$ ), previously proposed for the magnetic structure of Fe<sub>7</sub>S<sub>8</sub>. This suggests that the magnetic structure belongs to one of two possible magnetic representations ( $\Gamma_1$  or  $\Gamma_3$ ). Furthermore, interlayer antiferromagnetic exchange requires the four magnetic sublattices,  $\mathbf{m}_i$  ( $i=1,4$ ), where the subscript refers to the relevant cation site, to be coupled according to:

$$\mathbf{m}_1 - \mathbf{m}_2 + \mathbf{m}_3 - \mathbf{m}_4.$$

These conclusions were verified by applying a reverse Monte Carlo procedure to the screening of symmetry-allowed magnetic structures,<sup>18</sup> considering each of the basis vectors in turn. Subsequent least-squares refinement indicated that  $\Gamma_3(F_x)$  offered the best agreement with observed data and all subsequent refinement of the magnetic structure was based on this solution. Since the first-order crystallographic transition introduces odd terms into the exchange Hamiltonian, allowing admixture of other modes that span the same representation, ( $G_y$  and  $F_z$  in the present case), a trial magnetic structure was constructed in which there is intralayer ferromagnetic alignment of the  $\mu_x$  and  $\mu_z$

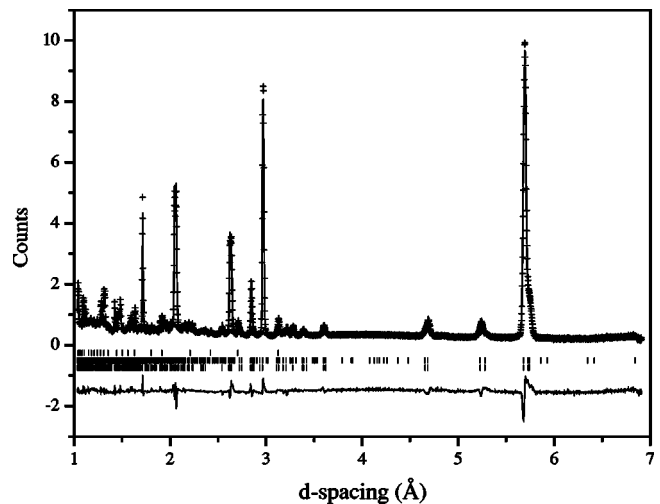


FIG. 2. Final observed (crosses), calculated (full line), and difference (lower full line) neutron profiles for Fe<sub>7</sub>S<sub>8</sub> collected on the Osiris diffractometer at 11 K. Reflection positions are marked: the lower markers refer to the crystallographic unit cell, the middle markers the magnetic unit cell described in the primitive space group  $P1$ , and the upper markers to the FeS<sub>2</sub> impurity phase.

magnetic-vector components and antiferromagnetic alignment of the  $\mu_y$  components. The magnetic structure was described in the primitive space group  $P1$  and the free-ion form factor<sup>22</sup> for Fe<sup>2+</sup> was used to describe the wavelength dependence of the magnetic scattering. With the exception of Fe(4), whose  $\mu_y$  magnetic-vector component in this representation is zero, all three magnetic vector components associated with each of the crystallographically distinct cations were initially set to nonzero values. The magnetic moments at each of the cation sites were constrained to be equal. During the early cycles of refinement, the  $\mu_y$  component of the moments refined to a value close to zero, the value at which it was subsequently fixed. The peak shape was modeled using a convolution of an Ikeda-Carpenter and a pseudo-Voigt function with the coefficients included as refinable parameters. Again an overall thermal parameter was used and a wavelength dependent absorption correction was included in the final cycles of refinement which involved 48 variables and resulted in the final observed, calculated and difference profiles of Fig. 2. The refined parameters appear in Table I while the magnetic structure at 11 K is shown in Fig. 3.

Data in the range  $2.7 \leq d(\text{Å}) \leq 6.0$  collected on Osiris were used to follow the evolution of the magnetic structure with temperature between 11 K and 413 K. The strong magnetic reflection at ca. 5.7 Å exhibits a smooth decrease in intensity with increasing temperature to 413 K (Fig. 4) with no evidence of the spin reorientation transition that has been reported for the analogous selenide.<sup>23,24</sup>

The structural parameters determined at 11 K were used for the trial nuclear and magnetic structures for the analysis of the data collected at 298 K using GEM. The refinement procedure was similar to that applied to the analysis of the Osiris data, with the exception of the simultaneous use of data from four detector banks in Rietveld refinement. The refined magnetic structure is similar to that determined at

TABLE I. Refined parameters for  $\text{Fe}_7\text{S}_8$  determined from data collected at 11 K on Osiris and at 298 K on GEM (space group  $C2/c$ ). Parentheses and square brackets denote cation sites in the vacancy and fully occupied layers, respectively. All atoms on  $8(f):(x,y,z)$  except for (Fe(4)) on  $4(e)$   $(0,y,1/4)$ .

	Temperature	
	11 K	298 K
$a(\text{Å})$	11.8656(4)	11.9258(2)
$b(\text{Å})$	6.8482(2)	6.8822(1)
$c(\text{Å})$	12.8958(3)	12.9245(2)
$\beta(^{\circ})$	118.075(2)	118.015(1)
$B(\text{Å}^2)$	0.94(4)	0.73(1)
Moment/ $\mu_B$	3.16(1)	2.993(5)
[Fe(1)]		
$x$	0.1268(5)	0.1260(2)
$y$	0.103(1)	0.0981(4)
$z$	0.9902(4)	0.9908(1)
$\mu_x$	2.75(1)	2.979(5)
$\mu_y$	0	0
$\mu_z$	-1.54(2)	-0.29(3)
(Fe(2))		
$x$	0.2560(6)	0.2560(2)
$y$	0.119(2)	0.1266(6)
$z$	0.2469(4)	0.2462(2)
$\mu_x$	-2.75(1)	-2.979(5)
$\mu_y$	0	0
$\mu_z$	1.54(2)	0.29(3)
[Fe(3)]		
$x$	0.3610(4)	0.3594(2)
$y$	0.144(1)	0.1401(5)
$z$	0.5047(4)	0.5000(2)
$\mu_x$	2.75(1)	2.979(5)
$\mu_y$	0	0
$\mu_z$	-1.54(2)	-0.29(3)
(Fe(4))		
$y$	0.378(2)	0.3931(5)
$\mu_x$	-2.75(1)	-2.979(5)
$\mu_y$	0	0
$\mu_z$	1.54(2)	0.29(3)
S(5)		
$x$	0.905(2)	0.8957(8)
$y$	0.125(7)	0.1228(2)
$z$	0.884(1)	0.8755(7)
S(6)		
$x$	0.349(2)	0.3531(8)
$y$	0.126(6)	0.1251(2)
$z$	0.114(1)	0.1234(6)
S(7)		
$x$	0.854(1)	0.8601(7)
$y$	0.126(6)	0.1254(1)
$z$	0.139(1)	0.1378(5)
S(8)		
$x$	0.601(2)	0.6024(9)
$y$	0.131(7)	0.1241(2)
$z$	0.619(1)	0.6206(7)
$R_{wp}$ (%)	7.0	5.1 (Bank 5: $2\theta=154^{\circ}$ ) 5.6 (Bank 4: $2\theta=91^{\circ}$ ) 5.0 (Bank 3: $2\theta=63^{\circ}$ ) 6.4 (Bank 2: $2\theta=17^{\circ}$ )

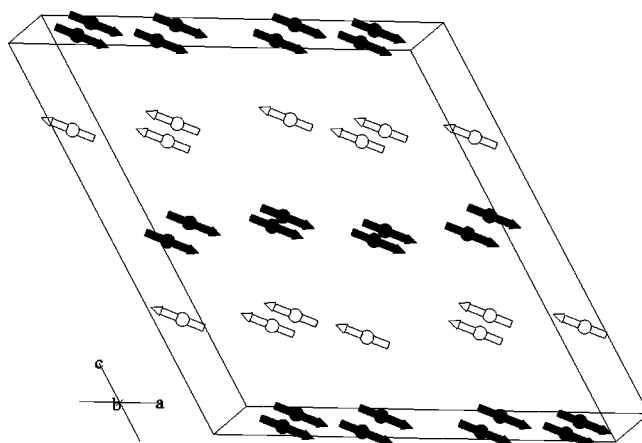


FIG. 3. A representation of the magnetic structure of  $\text{Fe}_7\text{S}_8$  at 11 K. Sulfide ions are omitted for clarity. Solid arrows represent moments in the fully occupied layer and open arrows represent moments in the ordered-defect layer. The crystallographic and magnetic unit cells are coincident and are outlined.

low temperature, with a slightly reduced ordered moment of  $\mu=2.993(5)\mu_B$  and confirms that no significant spin reorientation takes place in the temperature range  $11 \leq T(\text{K}) \leq 298$ . Refined parameters are presented in Table I and final observed, calculated and difference profiles in Fig. 5. Selected distances and angles are given in Table II.

Powder neutron-diffraction data from the low angle ( $2\theta = 17^{\circ}$ ) GEM detector bank, collected at temperatures in the range  $298 \leq T(\text{K}) \leq 773$  are plotted in Fig. 6(a), in which the evolution of the magnetic peaks with temperature may be clearly observed. The magnetic ordering temperature was established by plotting the intensity of the strong  $(001)_{\text{NiAs}}$

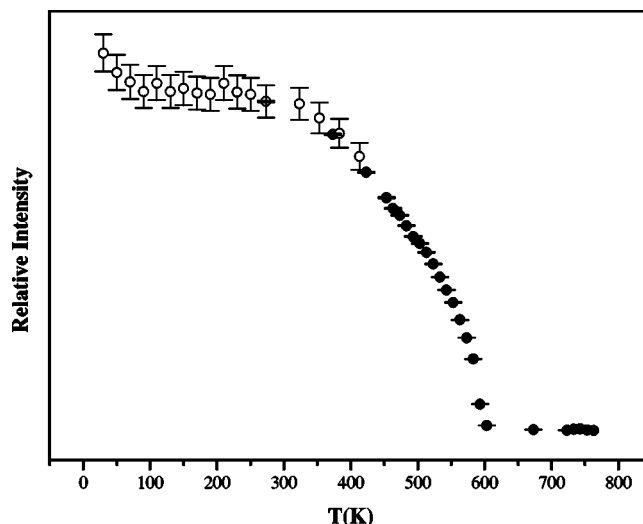


FIG. 4. The relative intensity of the  $(001)_{\text{NiAs}}$  magnetic reflection as a function of temperature. Intensity data obtained with the GEM (solid points) and Osiris (open points) diffractometers are normalized to the measured intensity at 273 K. Error bars for GEM data are within the points; the larger error bars associated with the Osiris data reflect the poorer statistics obtained with short data collection times on this instrument.

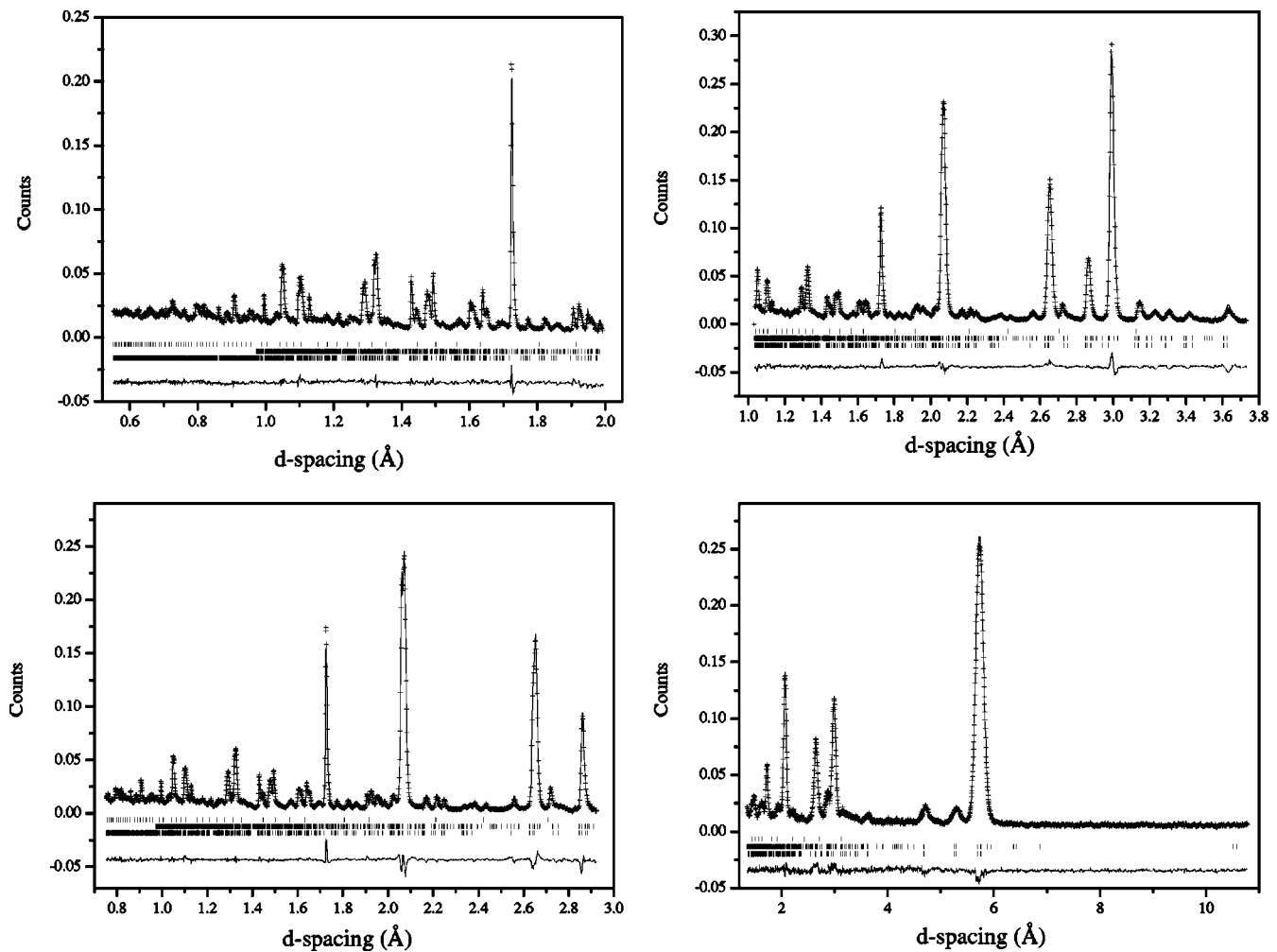


FIG. 5. Final observed (crosses), calculated (full line) and difference (lower full line) neutron profiles for each of the four GEM detector banks for refinements carried out using data collected at 298 K. Reflection positions are marked: the lower markers refer to the crystallographic unit cell, the middle markers to the magnetic unit cell described in the primitive space group  $P1$  and the upper markers to the  $\text{FeS}_2$  impurity phase.

magnetic reflection at  $d \approx 5.7 \text{ \AA}$  as a function of temperature (Fig. 4), leading to an estimate of  $T_N = 598(5) \text{ K}$ , in excellent agreement with that determined from the magnetization measurements, which show a marked increase on cooling below 600 K (Fig. 7). The magnetic intensity shows only a small degree of hysteresis. Examination of data from the high-resolution backscattering ( $2\theta = 154.4^\circ$ ) bank [Fig. 6(b)] demonstrates that on heating, the monoclinic distortion, as evidenced by splitting of the (102) reflection, indexed on the primitive NiAs unit cell, in the range  $2.0 \leq d(\text{\AA}) \leq 2.12$  is progressively removed, disappearing in the region of the magnetic ordering temperature. Detailed investigation of the evolution of nuclear and magnetic structures was undertaken by performing sequential Rietveld refinement on data from the four GEM detector banks over the entire temperature range studied. Diffraction patterns at temperatures up to 583 K were well fitted by the monoclinic 4C nuclear and magnetic structure determined at lower temperatures. At 593 K, refinement with a fully ordered 4C structure was unstable until partial occupancy of iron at the normally vacant  $4(e) (0, y, 1/4)$  site in the ordered-defect layer was intro-

duced. The occupancy of this site was refined with the constraint that the number of cations in the defect layer remained constant. At 593 K, this site is ca. 38% occupied, indicative of a relatively high degree of intralayer cation disorder as the structural transition is approached. Magnetic scattering is absent from the diffraction pattern collected at 603 K and the data cannot be accounted for using a monoclinic structure. A hexagonal cation-deficient NiAs structure was fitted to patterns collected above 603 K. Final observed, calculated and difference profiles at 773 K, the highest temperature at which data were collected, are shown in Fig. 8, while refined parameters are presented in Table III. Significant bond distances and angles appear in Table IV.

The same cation-deficient structure was refined to the data collected on cooling. Although the monoclinic distortion reappears on cooling through the structural transition, refinements on the basis of a completely ordered 4C structure are of poorer quality ( $\chi^2 \approx 7$ ) than those obtained using data collected on heating. This feature persists to the lowest temperature at which data were collected. The introduction of intralayer disorder produced a significant improvement in the quality of the refinement ( $\chi^2 \approx 4$ ) for all patterns collected at

TABLE II. Bond distances (Å) and angles (°) for Fe<sub>7</sub>S<sub>8</sub> determined from data collected on GEM at 298 K.

Bond	
Fe(1)-S(5)	2.439(9)
	2.405(10)
Fe(1)-S(6)	2.438(8)
	2.492(10)
Fe(1)-S(7)	2.327(9)
Fe(1)-S(8)	2.645(10)
Mean Fe(1)-S	2.46
Fe(2)-S(5)	2.454(11)
	2.435(11)
Fe(2)-S(6)	2.364(9)
Fe(2)-S(7)	2.473(8)
Fe(2)-S(8)	2.461(10)
	2.478(11)
Mean Fe(2)-S	2.44
Fe(3)-S(5)	2.496(10)
Fe(3)-S(6)	2.448(10)
Fe(3)-S(7)	2.378(7)
	2.400(9)
Fe(3)-S(8)	2.569(9)
	2.571(9)
Mean Fe(3)-S	2.48
Fe(4)-S(6)	2.367(10) × 2
Fe(4)-S(7)	2.452(9) × 2
Fe(4)-S(8)	2.494(9) × 2
Mean Fe(4)-S	2.44
Fe(1)-Fe(2)	2.921(3)
Fe(1)-Fe(3)	3.183(3)
	3.156(3)
Fe(2)-Fe(3)	2.914(3)
Fe(3)-Fe(3)	3.016(4)
Fe(3)-Fe(4)	2.866(2)
Angle	
S(5)-Fe(1)-S(5)	90.7(3)
S(5)-Fe(1)-S(6)	89.0(3)
	90.1(3)
S(5)-Fe(1)-S(7)	92.7(3)
	99.4(4)
S(5)-Fe(1)-S(8)	85.0(3)
	85.5(3)
S(6)-Fe(1)-S(6)	88.3(3)
S(6)-Fe(1)-S(7)	97.2(3)
	91.3(3)

TABLE II. (Continued.)

S(6)-Fe(1)-S(8)	85.0(3)
	83.9(3)
S(5)-Fe(2)-S(6)	90.7(3)
	94.1(3)
S(5)-Fe(2)-S(7)	86.1(3)
	89.1(3)
S(5)-Fe(2)-S(8)	90.9(4) × 2
	88.2(3)
	89.6(3)
S(6)-Fe(2)-S(8)	94.3(3)
	90.4(3)
S(7)-Fe(2)-S(8)	88.3(3)
	87.0(3)
S(5)-Fe(3)-S(7)	90.5(3)
	95.6(3)
S(5)-Fe(3)-S(8)	86.0(3)
	86.4(3)
S(6)-Fe(3)-S(7)	95.5(3)
	90.5(3)
S(6)-Fe(3)-S(8)	86.8(3)
	86.4(3)
S(7)-Fe(3)-S(7)	101.7(4)
S(7)-Fe(3)-S(8)	87.8(3)
	88.2(3)
S(8)-Fe(3)-S(8)	82.4(3)
S(6)-Fe(4)-S(6)	95.2(5)
S(6)-Fe(4)-S(7)	91.2(2) × 2
S(6)-Fe(4)-S(8)	93.4(3) × 2
	90.3(3) × 2
S(7)-Fe(4)-S(7)	82.5(4)
S(7)-Fe(4)-S(8)	87.1(3) × 2
	88.8(3) × 2

lower temperatures, on cooling. At 573 K the occupancy of the 4(*e*) site is ca. 34% and remains as high as 25% down to the lowest temperature studied.

There are marked anomalies in all unit-cell parameters on passing through the magnetic and structural transition (Fig. 9). No such anomalies or thermal hysteresis were observed in the cubic lattice parameter of the pyrites impurity phase, indicating that the sample was thermally equilibrated at each temperature. The *a* and *b* parameters of Fe<sub>7</sub>S<sub>8</sub> show a discontinuity at ca. 600 K, characteristic of a first-order transition while *c* and  $\beta$  exhibit a more complicated thermal history dependence. Calculation of the thermal expansion tensor and its temperature dependence shows that whilst the *b* axis exhibits normal Grüneisen behavior, the maximum and minimum principal axes in (010) show maxima at ~220 K and ~290 K, respectively, before reducing in magnitude towards

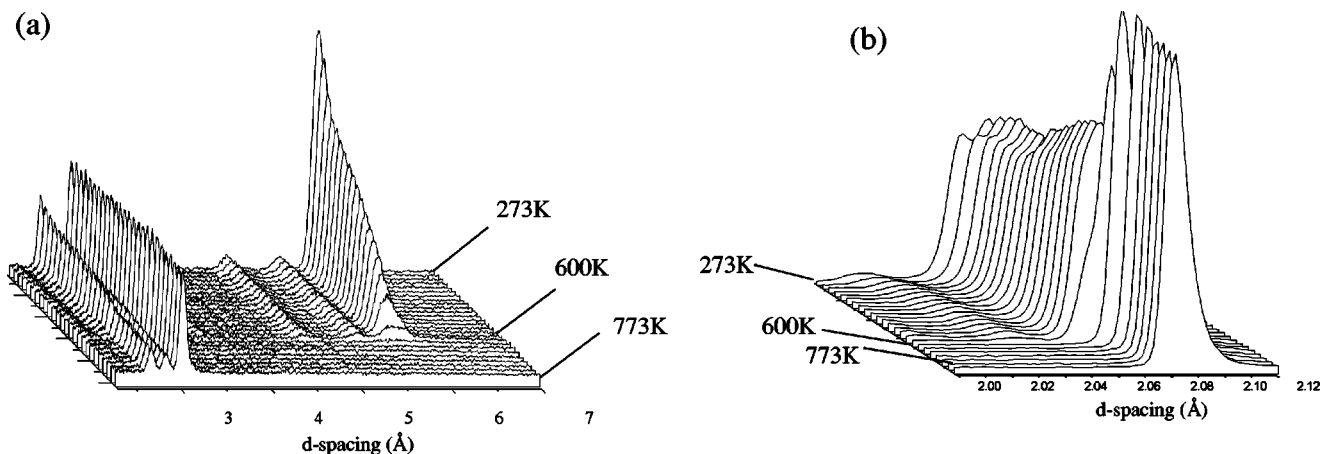


FIG. 6. Powder neutron-diffraction data from (a) the low-angle GEM detector bank over the temperature range  $298 \leq T(\text{K}) \leq 773$ , illustrating the collapse of the magnetic intensity associated with the  $(001)_{\text{NiAs}}$  reflection at  $T \geq 603$  K and (b) the backscattering GEM detector bank showing the concomitant removal of the monoclinic distortion, as evidenced by disappearance of the splitting of the  $(102)_{\text{NiAs}}$  crystallographic reflection.

the Curie temperature. The change in orientation of the thermal expansion tensor as a function of temperature mirrors the variation in moment orientation, with the two directions being separated by only  $10^\circ$  at 298 K. Magnetostrictive effects thus clearly dominate the temperature dependence of the unit-cell parameters within the ferrimagnetic phase. Comparison (Fig. 9) of the temperature dependence of the ordered moment  $\mu$  and the angle  $\beta$  clearly shows that the loss of long-range magnetic order is coincident with the removal of the monoclinic distortion.

#### IV. DISCUSSION

At  $T \leq 593$  K,  $\text{Fe}_7\text{S}_8$  adopts a monoclinic structure, in which cation-deficient and fully occupied layers alternate. The former are stacked in an ABCD sequence in a direction perpendicular to the cation layers, giving rise to the designation as a 4C structure. The ideal dichalcogenide block has hexagonal symmetry, which would give each cation six equi-

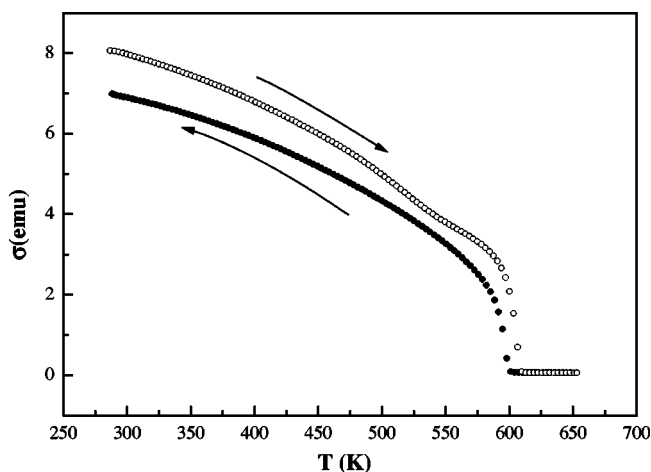


FIG. 7. Magnetization data for  $\text{Fe}_7\text{S}_8$  collected on heating (open points) and cooling (solid points) in a measuring field of 100 G.

distant cation neighbors within the layer. Rietveld refinement using data collected at 298 K reveals a marked distortion of the fully occupied layer in  $\text{Fe}_7\text{S}_8$ , with both long ( $>3.8$  Å) and short ( $<3.0$  Å) intralayer Fe-Fe distances being observed. An empirical estimate<sup>25</sup> of the critical distance  $R_C$  for direct  $t_{2g}$ - $t_{2g}$  orbital overlap is ca. 3.4 Å for Fe(II) in a sulphide matrix. This suggests that within the fully occupied layer there are distorted [ $r(\text{Fe1-Fe3})/r(\text{Fe3-Fe3}) > 1$ ] diamondlike clusters (Fig. 10), in which cation-cation separations are significantly shorter than  $R_C$ , suggesting a moderate degree of cation-cation interaction, while a shortest intercluster distance of 3.404(5) Å (at room temperature) indicates considerably weaker interactions between individual clusters. Clustering of cations within the dichalcogenide block has been observed in a range of ordered-defect sulphides. Diamond, zigzag, and triangular clustering schemes have been described<sup>26–28</sup> and Canadell *et al.*<sup>29</sup> have shown that there is a relationship between the nature of the distortion and the electrical transport properties of materials containing  $\text{MS}_2$  units. The isolated nature of the diamond clusters observed here is consistent with the semiconducting behavior of  $\text{Fe}_7\text{S}_8$ . At elevated temperatures, interlayer disordering of cations leads to a transition to a cation-deficient NiAs structure. The transition temperature is determined as 598(5) K, from the temperature dependence of the monoclinic angle  $\beta$ , and the marked anomalies in the lattice parameters. Although all intracluster distances increase due to thermal expansion, the cluster remains distorted to 583 K, above which temperature, the distances increase rapidly, attaining identical values at the structural transition to the NiAs phase [Fig. 11(a)]. Examination of the interlayer cation-cation distances as a function of temperature [Fig. 11(b)] indicates that the marked nonplanarity of the cation layers in the monoclinic phase disappears on transformation to the NiAs structure.

On the basis of x-ray diffraction and DTA measurements the following sequence of phase transitions with increasing temperature has been proposed<sup>12</sup> for monoclinic  $\text{Fe}_7\text{S}_8$

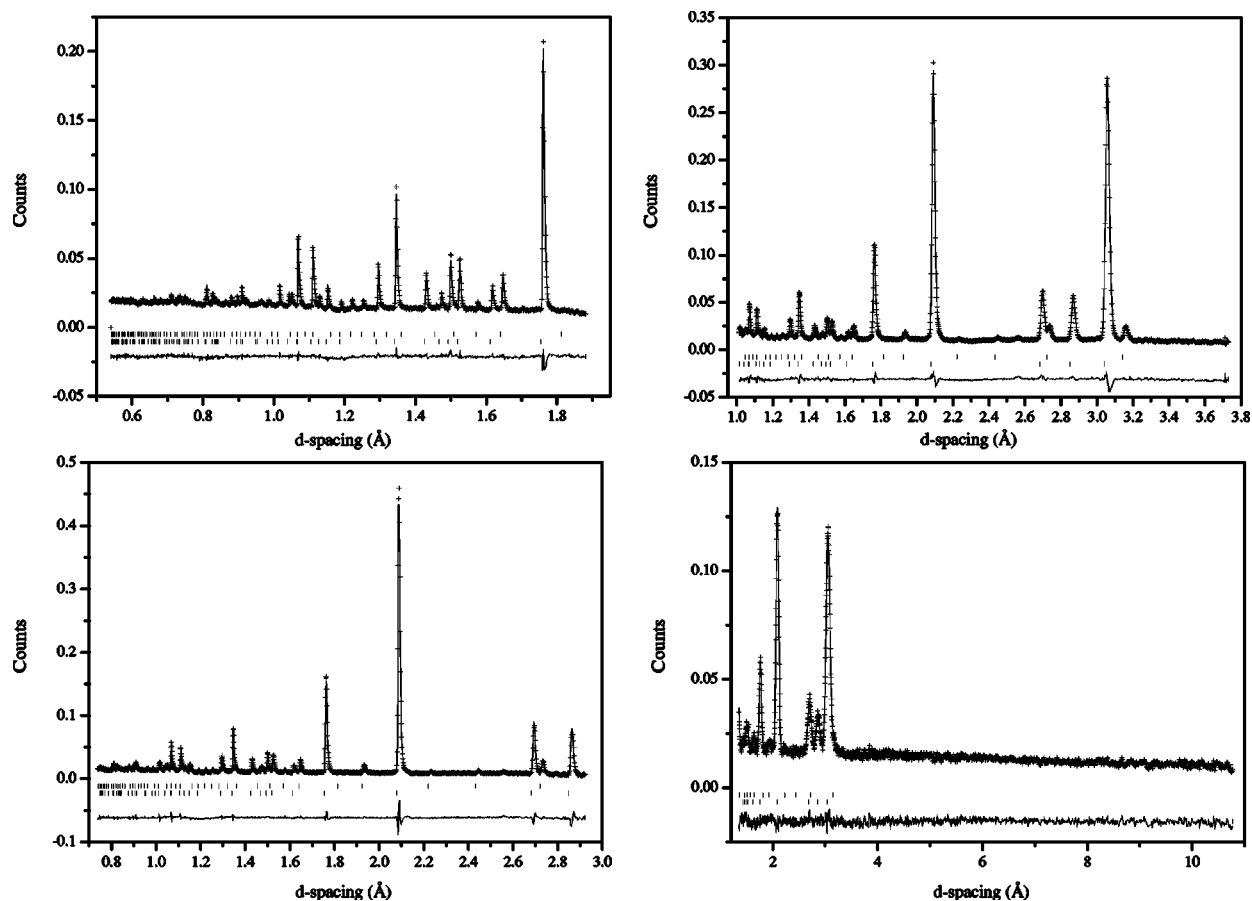


FIG. 8. Final observed (crosses), calculated (full line), and difference (lower full line) neutron profiles for each of the four GEM detector banks for refinements carried out using data collected at 773 K. Reflection positions are marked: the lower markers refer to  $\text{Fe}_7\text{S}_8$  and the upper markers the  $\text{FeS}_2$  impurity phase.

monoclinic(4C)  $\rightarrow$  trigonal(3C)  
 $\rightarrow$   $\text{CdI}_2$ -type (intralayer disorder),

while at higher temperatures, formation of a NiAs-type phase through interlayer disorder has been reported.<sup>11</sup> Analysis of neutron-diffraction data presented here suggests that partial intralayer disordering of cations occurs at temperatures below that of the  $4\text{C} \rightarrow \text{NiAs}$  transition, although this remains

TABLE III. Refined parameters for  $\text{Fe}_7\text{S}_8$  (space group  $P6_3/mmc$ ) determined from data collected on GEM at 773 K [Fe on  $2(a)$  (0,0,0); S on  $2(d)$  ( $1/3, 2/3, 3/4$ )].

	$a(\text{Å})$	3.51647(2)
	$c(\text{Å})$	5.71422(6)
Fe	SOF	0.88(−)
	$B(\text{Å}^2)$	3.79(2)
S	$B(\text{Å}^2)$	2.35(3)
$R_{\text{wp}}$ (%)		4.1 (Bank 5: $2\theta=154^\circ$ )
		5.6 (Bank 4: $2\theta=91^\circ$ )
		5.0 (Bank 3: $2\theta=63^\circ$ )
		6.4 (Bank 2: $2\theta=17^\circ$ )

incomplete and the absence of  $(00\ell)$  reflections with  $\ell=2n+1$  indicates the absence of an intermediate  $\text{CdI}_2$ -like phase.

While  $\text{CdI}_2$ -type intermediates have been identified in analogous ordered-defect materials such as  $\text{V}_3\text{S}_4$  and  $\text{Fe}_{1.8}\text{V}_{1.2}\text{S}_{3.93}$ , it has been shown that the transition temperature,  $T_c$ , for the  $\text{CdI}_2$  to the NiAs phase change for a system  $M_{1-\delta}X$  is dependent both on composition, with the stability of the  $\text{CdI}_2$ -type phase decreasing with decreasing defect concentration, and on the ratio of the interlayer ( $\epsilon'_{vv}$ ) to intralayer ( $\epsilon''_{vv}$ ) vacancy-vacancy interaction energies. The absence of a  $\text{CdI}_2$ -type phase for  $\text{Fe}_7\text{S}_8$  implies  $\epsilon'_{vv} \approx 3\epsilon''_{vv}$ , as

TABLE IV. Bond distances (Å) and angles ( $^\circ$ ) for  $\text{Fe}_7\text{S}_8$  determined from data collected on GEM at 773 K.

Bond	
Fe-S	$2.48247(1) \times 6$
Fe-Fe	$3.51647(2) \times 6$
	$2.85711(3) \times 2$
Angle	
S-Fe-S	$90.187(0) \times 6$
	$89.813(0) \times 6$

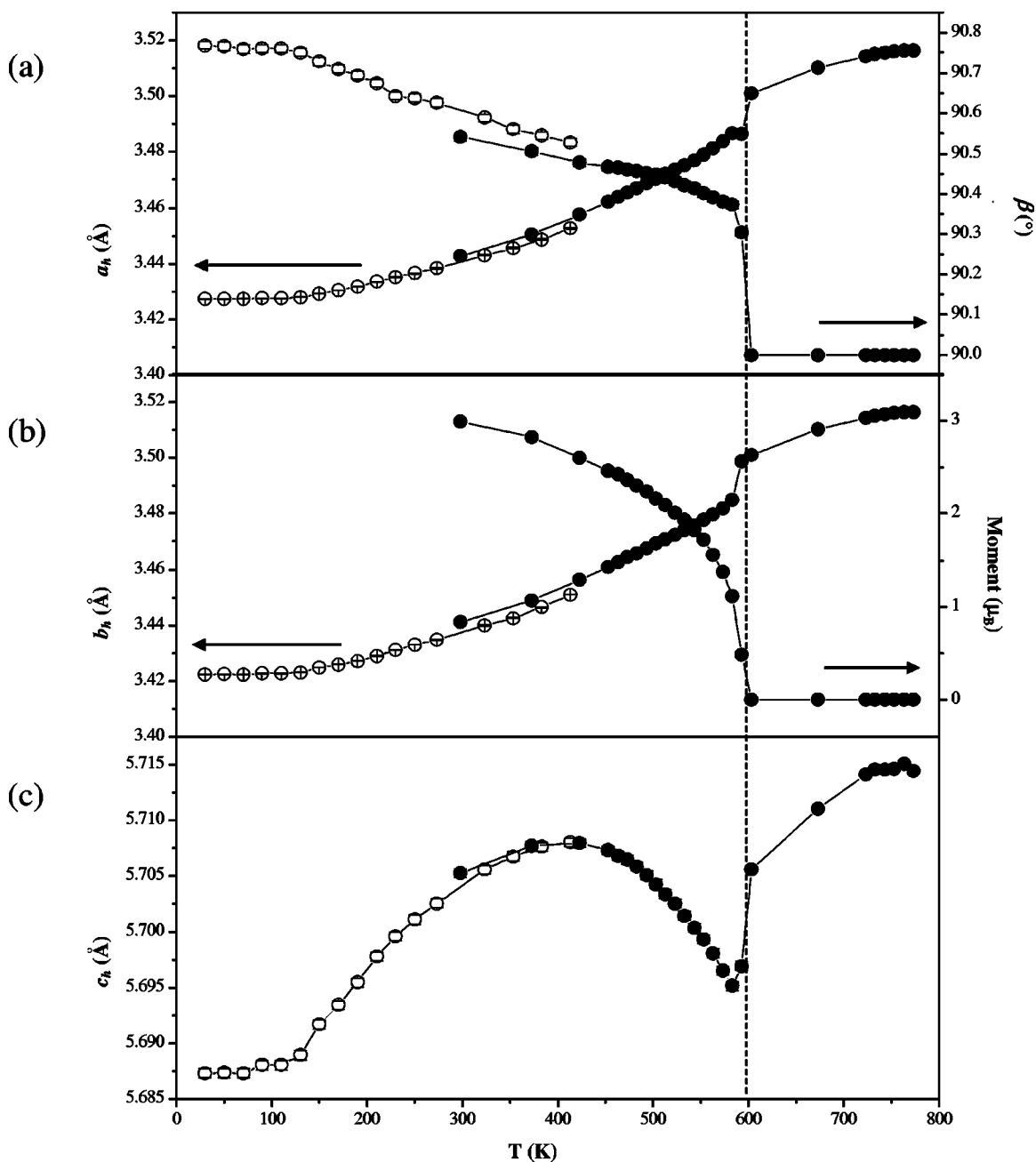


FIG. 9. The temperature dependence of the unit-cell parameters (a)  $a$  and  $\beta$ , (b)  $b$ , and (c)  $c$ . To aid comparison, lattice parameters for the monoclinic  $\text{Fe}_7\text{S}_8$  are referred to the hexagonal NiAs unit cell ( $a_m \approx 2\sqrt{3}a_h, b_m \approx 2b_h$ , and  $c_m \approx 4c_h$ ). The temperature variation of the ordered moment is included in (b) in order to demonstrate the coincidence of the magnetic and structural transitions. Open points derive from data collected on Osiris while solid points are from the data collected on GEM. Solid lines are a guide to the eye, while the dashed vertical line indicates the magnetic ordering temperature determined from the magnetization data. In some instances, error bars lie within the points.

appears to be the case in the ordered-defect phase  $\text{NiCr}_2\text{S}_4$ .<sup>6,30</sup>

The neutron diffraction pattern of a phase with the 3C structure differs sufficiently from that of a material with the 4C structure that any change in stacking sequence would be immediately apparent. No such change was observed and contrary to the conclusions of Li *et al.*,<sup>10</sup> our data clearly demonstrate that the 4C structure transforms directly to a defective NiAs structure with a simultaneous loss of long-range magnetic order. This difference may be associated with

the nature of the experimental procedures. All of the structural and thermal measurements of Li *et al.*<sup>10</sup> were made on samples contained either in vacuum or in flowing gas. Under such conditions, mixed-metal sulphides commonly evolve sulphur at elevated temperatures, leading to a change in stoichiometry which may have a marked influence on the phase behavior. Indeed, at temperatures in excess of 823 K marked changes in the magnetic properties of  $\text{Fe}_7\text{S}_8$  were reported, while we have observed<sup>30</sup> that loss of sulphur from  $\text{NiCr}_2\text{S}_4$  at high temperatures renders the order-disorder transition ir-

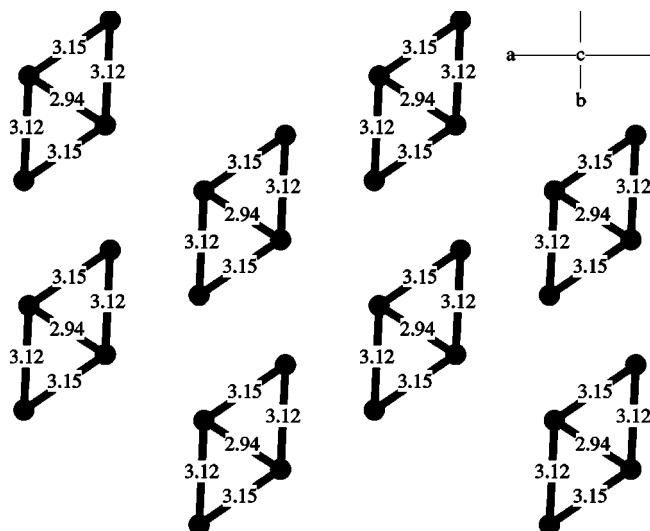


FIG. 10. View along [001] of the arrangement of cations in the fully occupied layer of  $\text{Fe}_7\text{S}_8$  determined from powder neutron diffraction at 11 K. Solid lines indicate short Fe-Fe distances at the distances marked, illustrating the diamond-type clusters referred to in the text.

reversible but reversibility is retained when the sample is contained in an evacuated sealed silica tube, as used in the present work. Furthermore the properties of synthetic pyrrhotite are sensitively dependent on the degree of cation ordering. The sample of  $\text{Fe}_7\text{S}_8$  synthesized in this work, produced a powder-diffraction pattern that prior to heating, exhibited no sign of the stacking faults reported by Li *et al.*<sup>10</sup> (the monoclinic splitting was clearly visible) or of any significant intralayer disorder.

The refined magnetic structure (Fig. 3) comprises sheets parallel to the (001) crystallographic plane of ferromagnetically aligned moments with antiferromagnetic coupling between neighboring sheets along the [001] direction. The magnetic moments lie in the (010) plane and are directed at an angle of ca.  $6^\circ$  to the plane of the iron atoms that comprise the fully occupied and cation-deficient layers. On cooling below room temperature, the  $\mu_z$  component of the magnetic moment increases, and at 11 K the moments are directed at an angle of ca.  $29^\circ$  to the iron layers. The analogous selenide shows a more marked spin reorientation below ambient temperature.<sup>24</sup> Examination of the temperature dependence of the integrated intensity of the  $(001)_{\text{NiAs}}$  reflection of  $\text{Fe}_7\text{S}_8$  indicates that on cooling below 220 K, the moment slowly rotates out of the (001) crystallographic plane, reaching an angle of ca.  $70^\circ$  to this plane at the lowest temperature studied.

In the magnetic structure determined here, an identical magnetic moment is associated with each of the four crystallographically distinct iron sites. Bertaut<sup>19</sup> formulated  $\text{Fe}_7\text{S}_8$  as an ionic species  $(\text{Fe}_2^{3+}\text{Fe}_5^{2+}\text{S}_8)$  and determined the electrostatic stabilization energy for different distributions of  $\text{Fe}^{3+}$  over the two types of layer. The energetically most favorable configuration is that in which  $\text{Fe}^{3+}$  occupies sites in both vacancy and fully occupied layers. However, this arrangement does not produce agreement with the observed saturation magnetization of  $2.03\mu_B$  per formula unit, assum-

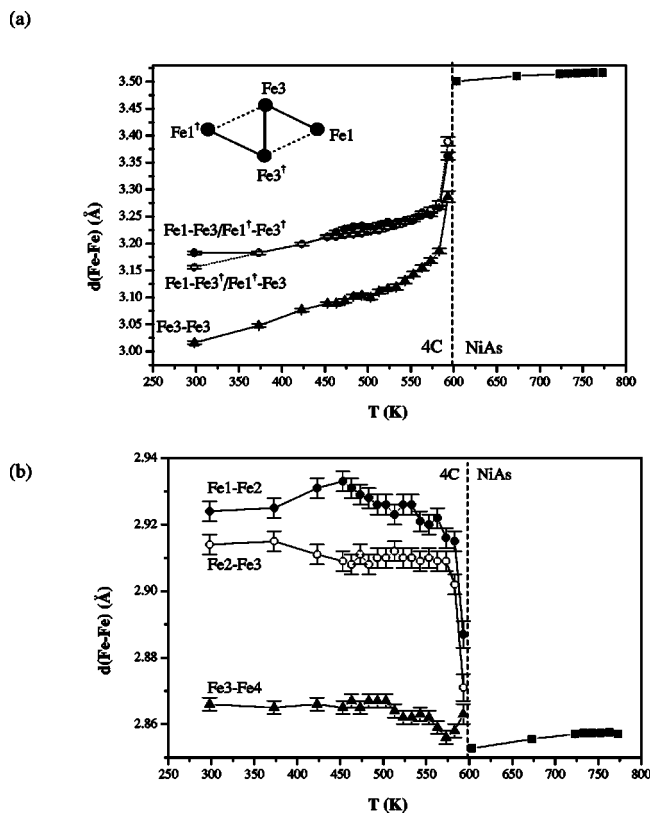


FIG. 11. The temperature variation over the range  $298 \leq T(\text{K}) \leq 773$  of (a) the intralayer Fe-Fe distances within the fully occupied layer of  $\text{Fe}_7\text{S}_8$  and (b) the interlayer Fe-Fe distances over the same range of temperature. For the high-temperature phase, error bars are within the points.

ing spin-only behavior for the  $\text{Fe}^{2+}$  and  $\text{Fe}^{3+}$  moments. Indeed, the best agreement corresponds to a configuration  $(\text{Fe}_2^{3+}\text{Fe}_5^{2+})[\text{Fe}_4^{2+}]\text{S}_8$  in which  $\text{Fe}^{3+}$  ions are confined to the vacancy layers. Kawaminami and Okazaki in a study of the analogous selenide<sup>24</sup> suggest that the agreement with the magnetization data may be fortuitous and a saturation value of  $2\mu_B$  per formula unit can be accounted for by a model in which all moments are equivalent and which for  $\text{Fe}_7\text{S}_8$  also gives better agreement with neutron-diffraction data than does the ionic model. This is consistent with the results obtained here for  $\text{Fe}_7\text{S}_8$  and suggests that the electron transfer is sufficiently rapid that individual valence states cannot be distinguished. This is supported by Mössbauer experiments<sup>31,32</sup> that show no indication of  $\text{Fe}^{3+}$  even at 4.2 K, suggesting that the material is better formulated as  $\text{Fe}_7^{2.29+}\text{S}_8$ , which would lead to an ordered moment of  $4.29\mu_B$  per cation (or  $4.23\mu_B$  when nonstoichiometry arising from the  $\text{FeS}_2$  impurity is taken into account). The ordered moment of  $3.16(1)\mu_B$  determined here represents a reduction to ca. 74% of the spin-only value. Such a reduction is comparable with that observed in related materials<sup>33-35</sup> and may be attributed to the transfer of spin from the cation owing to the covalency of the Fe-S interactions.

#### ACKNOWLEDGMENT

A.V.P. thanks The Royal Society of Edinburgh for financial support.

TABLE V. Irreducible representations of the little group  $G_k$  and the characters of the permutation, axial vector, and magnetic representations associated with the  $8(f)$  and  $4(e)$  Wyckoff sites.

	$\{1 000\}$	$\{2_y 000.5\}$	$\{\bar{1} 000\}$	$\{m_y 000.5\}$
$\Gamma_1$	1	1	1	1
$\Gamma_2$	1	1	-1	-1
$\Gamma_3$	1	-1	1	-1
$\Gamma_3$	1	-1	-1	1
8(f) site				
$\Gamma_{\text{perm}}$	4	0	0	0
$\tilde{V}$	3	-1	3	-1
$\Gamma_{\text{mag}}$	12	0	0	0
4(e) site				
$\Gamma_{\text{perm}}$	2	2	0	0
$\tilde{V}$	3	-1	3	-1
$\Gamma_{\text{mag}}$	6	-2	0	0

#### APPENDIX: GROUP THEORETICAL ANALYSIS OF THE MAGNETIC STRUCTURE of $\text{Fe}_7\text{S}_8$

The possible magnetic structures compatible with the  $C2/c$  symmetry of  $\text{Fe}_7\text{S}_8$  were determined through the method of representational analysis described by Bertaut.<sup>17</sup> For a propagation vector  $\mathbf{k}=(0,0,0)$ , the little group  $G_k$ , formed by those space group elements that leave  $\mathbf{k}$  invariant, coincides with the space group  $G_0$ . The irreducible representations of the little group  $G_k$  are shown in Table V, where the symmetry elements are represented in the notation of the International Tables.<sup>36</sup>

A symmetry operator,  $g=\{R|\tau\}$ , where  $R$  and  $\tau$  refer, respectively, to rotational and translational components, acts on both the position of the atom and on the components of the axial vector that describes the moment. As the lattice is  $C$  centered, half of the positions associated with each cation site are generated by a lattice translation only. Therefore, consideration of the action of the symmetry operations may be confined to those positions that are generated by the four operations of Table V, since inclusion of the effects of lattice centering requires only a scaling of the results. Consideration of each symmetry operation in turn acting on the atomic positions generates a permutation representation  $\Gamma_{\text{perm}}$ , and on the spin components, an axial vector representation  $\tilde{V}$ , the

TABLE VI. Basis vectors spanned by each of the irreducible representations of the little group  $G_k$ .

Irreducible representation	Basis vectors	
	8(f) site	4(e) site
$\Gamma_1$	$G_x, F_y, G_z$	$F'_y$
$\Gamma_2$	$A_x, C_y, A_z$	$G'_y$
$\Gamma_3$	$F_x, G_y, F_z$	$F'_x, F'_z$
$\Gamma_4$	$C_x, A_y, C_z$	$G'_x, G'_z$
	$F=\mathbf{S}_1+\mathbf{S}_2+\mathbf{S}_3+\mathbf{S}_4$	$F'=\mathbf{S}_5+\mathbf{S}_6$
	$G=\mathbf{S}_1-\mathbf{S}_2+\mathbf{S}_3-\mathbf{S}_4$	$G'=\mathbf{S}_5-\mathbf{S}_6$
	$C=\mathbf{S}_1+\mathbf{S}_2-\mathbf{S}_3-\mathbf{S}_4$	
	$A=\mathbf{S}_1-\mathbf{S}_2-\mathbf{S}_3+\mathbf{S}_4$	

characters of both of which are contained in Table V. The magnetic representation at a given site,  $\Gamma_{\text{mag}}$ , is then given by the direct product.

$$\Gamma_{\text{mag}} = \tilde{V} \times \Gamma_{\text{perm}}. \quad (\text{A1})$$

This may then be reduced to a sum of irreducible representations of the little group,

$$\Gamma_{\text{mag}} = \sum_{\nu} n_{\nu} \Gamma_{\nu}, \quad (\text{A2})$$

where the number of times  $n_{\nu}$  that an irreducible representation  $\Gamma_{\nu}$  appears is given by

$$n_{\nu} = \frac{1}{n(G_k)} \sum_g \chi(g) \chi_{\nu}^*(g), \quad (\text{A3})$$

$\chi(g)$  is the character of the reducible representation under the symmetry operation  $g$  of the little group  $G_k$  and  $\chi_{\nu}(g)$  is the character of the irreducible representation  $\Gamma_{\nu}$  under the same symmetry operation. This gives rise to the irreducible magnetic representations used in the main body of the paper.

The cations at the  $8(f)$  site generated by the operations in Table V are denoted as (1)  $(x, y, z)$ ; (2)  $(-x, y, -z+1/2)$ ; (3)  $(-x, -y, -z)$ , and (4)  $(x, -y, z+1/2)$ , and those at the  $4(e)$  site by (5)  $(0, y, 1/4)$  and (6)  $(0, -y, 3/4)$ . Application of the projection operator<sup>37</sup> produces the basis vectors associated with each of the irreducible representations. The resulting basis vectors are denoted in Table VI, using a notation similar to that introduced by Bertaut<sup>17</sup> to identify the different linear combinations of spins  $\mathbf{S}_i$  at the  $i$ th cation position of a given a Wyckoff site.

\*Corresponding author. Present address: Department of Chemistry, Heriot-Watt University, Edinburgh EH14 4AS, UK. E-mail address: a.v.powell@hw.ac.uk

<sup>1</sup>P. Vaqueiro and A. V. Powell, Chem. Mater. **12**, 2705 (2000).

<sup>2</sup>Y. Oka, K. Kosuge, and S. Kachi, J. Solid State Chem. **23**, 11 (1978).

<sup>3</sup>T. Ohtani, R. Fujimoto, H. Yoshinaga, and M. Nakahira, J. Solid

State Chem. **48**, 161 (1983).

<sup>4</sup>Y. Oka, K. Kosuge, and S. Kachi, Mater. Res. Bull. **15**, 521 (1980).

<sup>5</sup>H. Wada, Bull. Chem. Soc. Jpn. **52**, 2918 (1979).

<sup>6</sup>P. Vaqueiro, S. Hull, B. Lebech, and A. V. Powell, J. Mater. Chem. **9**, 2859 (1999).

<sup>7</sup>D. J. Vaughan and J. R. Craig, Mineral Chemistry of Metal Sul-

- fidés* (CUP, Cambridge, 1978).
- <sup>8</sup>N. Moritomo, H Nakazawa, K. Nishiguchi, and M. Tokonami, *Science* **168**, 964 (1970).
- <sup>9</sup>L. Néel, *Rev. Mod. Phys.* **25**, 58 (1953).
- <sup>10</sup>F. Lotgering, *Philips Res. Rep.* **11**, 190 (1956).
- <sup>11</sup>F. Li and H. F. Franzen, *J. Solid State Chem.* **126**, 108 (1996).
- <sup>12</sup>F. Li, H. F. Franzen, and M. J. Kramer, *J. Solid State Chem.* **124**, 264 (1996).
- <sup>13</sup>W. G. Williams, R. M. Ibberson, P. Day, and J. E. Enderby, *Physica B* **241-243**, 234 (1998).
- <sup>14</sup>K. H. Andersen, D. Martin y Marero, and M. J. Barlow, *Appl. Phys. A: Mater. Sci. Process.* **74**, S237 (2002).
- <sup>15</sup>W. I. F. David, M. W. Johnson, K. J. Knowles, C. M. Moreton-Smith, G. D. Crosbie, E. P. Campbell, S. P. Graham, and J. S. Lyall, Rutherford Appleton Laboratory Report No. RAL-86-102 (1986).
- <sup>16</sup>A. C. Larson and R. B. von Dreele, Los Alamos Laboratory Report No. LAUR 85-748 (1994).
- <sup>17</sup>E. F. Bertaut, in *Magnetism*, edited by G. T. Rado and H. Suhl (Academic Press, New York, 1963), Vol. III, Chap. 4, p. 149.
- <sup>18</sup>A. S. Wills, *Physica B* **276**, 680 (2000).
- <sup>19</sup>E. F. Bertaut, *Acta Crystallogr.* **6**, 557 (1953).
- <sup>20</sup>M. Tokonami, K. Nishiguchi, and N. Moritomo, *Am. Mineral.* **57**, 1066 (1972).
- <sup>21</sup>E. F. Bertaut, *J. Magn. Magn. Mater.* **24**, 267 (1981).
- <sup>22</sup>P. J. Brown, in *International Tables for Crystallography*, edited by A. J. C. Wilson (Kluwer, Dordrecht, 1992), Vol. C, Chap. 4.
- <sup>23</sup>K. Hirakawa, *J. Phys. Soc. Jpn.* **12**, 929 (1957).
- <sup>24</sup>M. Kawaminami and A. Okazaki, *J. Phys. Soc. Jpn.* **29**, 649 (1970).
- <sup>25</sup>J. B. Goodenough, *Propriétés Thermodynamiques Physiques et Structurales des Dérivés Semi-Métalliques* (CNRS, Paris, 1967).
- <sup>26</sup>J. GuilleVIC, J.-Y. Le Marrouille, and D. Grandjean, *Acta Crystallogr., Sect. B: Struct. Crystallogr. Cryst. Chem.* **30**, 111 (1974).
- <sup>27</sup>P. Vaqueiro, M. L. Kosidowski, and A. V. Powell, *Chem. Mater.* **14**, 1201 (2002).
- <sup>28</sup>P. Vaqueiro, M. Bold, A. V. Powell, and C. Ritter, *Chem. Mater.* **12**, 1034 (2000).
- <sup>29</sup>E. Canadell, A. LeBeuze, M. Abdelaziz El Khalifa, R. Chevrel, and M.-H. Whangbo, *J. Am. Chem. Soc.* **111**, 3778 (1989).
- <sup>30</sup>P. Vaqueiro, S. Hull, B. Lebech, and A. V. Powell, *J. Mater. Chem.* **9**, 2859 (1999).
- <sup>31</sup>D. J. Vaughan and M. S. Ridout, *Solid State Commun.* **8**, 2165 (1970).
- <sup>32</sup>L. M. Levinson and D. Treves, *J. Phys. Chem. Solids* **29**, 2227 (1968).
- <sup>33</sup>A. V. Powell, D. C. Colgan, and C. Ritter, *J. Solid State Chem.* **110**, 134 (1997).
- <sup>34</sup>A. V. Powell, D. C. Colgan, and C. Ritter, *J. Solid State Chem.* **143**, 163 (1999).
- <sup>35</sup>T. Hamasaki, T. Hashimoto, Y. Yamaguchi, and H. Watanabe, *Solid State Commun.* **16**, 895 (1975).
- <sup>36</sup>*International Tables for Crystallography*, edited by T. Hahn (Kluwer, Dordrecht, 1992), Vol. A.
- <sup>37</sup>C. J. Bradley and A. P. Cracknell, *The Mathematical Theory of Symmetry in Solids* (Clarendon Press, Oxford, 1972).